Earth Planet. Sci. Lett. 672 (2025) 119622

Contents lists available at ScienceDirect

Earth and Planetary Science Letters

journal homepage: www.elsevier.com/locate/epsl

A microstructural signature of the coesite-quartz transformation: New insights from high-pressure experiments and EBSD

Rellie M. Goddard [a,1,*], Andrew J. Cross [a], Geoffrey E. Lloyd [b], Thomas Breithaupt [c], Kathryn M. Kumamoto [d], Brendan V. Dyck [e], Haiyan Chen [f], Andrew Parsons [g], Anna K. Bidgood [h]

[a] Department of Geology and Geophysics, Woods Hole Oceanographic Institution, Woods Hole, MA, USA
[b] School of Earth and Environment, University of Leeds, Leeds, UK
[c] Department of Earth Sciences, University of Cambridge, Cambridge, UK
[d] Lawrence Livermore National Laboratory, Livermore, CA, USA
[e] Department of Earth and Environmental Sciences, The University of British Columbia, Kelowna, Canada
[f] Mineral Physics Institute, Stony Brook University, Stony Brook, NY, USA
[g] School of Geography, Earth and Environmental Sciences, University of Plymouth, Plymouth, UK
[h] University College Dublin, School of Earth Sciences, O'Brien Centre for Science, Belfield, Ireland

ARTICLE INFO

Editor: Dr A Webb

Keywords:
Epitaxy
Crystallography
Quartz
Coesite
UHP
EBSD

ABSTRACT

Ultra-high pressure (UHP) metamorphism is difficult to identify in continental crust as few petrological barometers are suitable for dominantly felsic lithologies. In such cases, burial to extreme depths is commonly identified through the preservation of coesite, a high-pressure polymorph of SiO_2 that typically forms at depths exceeding ~ 100 km (i.e., > 2 GPa pressure). Unfortunately, coesite readily transforms to quartz upon exhumation, meaning that UHP terranes may often be overlooked. While some studies have suggested that quartz may inherit an orientation signature indicative of former coesite, both the specific nature of this signature and the conditions favouring its development remain uncertain. To address this problem, we combine electron backscatter diffraction analysis of natural and experimental samples to explore microstructural evolution across the coesite-quartz phase transformation. We demonstrate that neighbouring domains of quartz commonly feature an $84 \pm 4^{\circ}$ rotation of [c] axes around the pole of a common {m} plane. This orientation relationship is a product of epitaxy, whereby the $\{11\bar{2}2\}$ Japan twin plane in quartz nucleates on the (010) plane in coesite. In supercell simulations, the nucleation of Japan twins can be explained by the energetically favourable alignment of quartz tetrahedra on parental coesite tetrahedra. Through experiments, we demonstrate that this signature emerges over a broad range of conditions, regardless of the availability of nucleation sites (e.g., grain boundaries) or the density of crystal lattice defects (e.g., dislocations). Overall, our work provides a quantitative and unambiguous tool for identifying UHP terranes from quartz in isolation.

1. Introduction

Continental subduction is a fundamental geodynamic process that can cause significant changes in tectonic plate motions and configurations (e.g., Bidgood et al., 2024; Parsons et al., 2021; Wheeler et al., 2001). Ultra-high pressure (UHP) terranes provide evidence for exhumation of subducted material from depths of > 100 km (e.g., Warren, 2013) and, as such, are an important record of changes in the geodynamics of past continental subduction zones (e.g., Bidgood et al., 2024). However, UHP terranes are difficult to identify in continental crust due to the scarcity of petrological indicators of burial to UHP conditions in felsic rocks (e.g., Proyer, 2003). While recent developments in elastic geothermobarometry (e.g., Kohn, 2014) negate some of the issues with traditional barometers, they require the absence of plastic flow and/or cracking, both of which are common during exhumation.

* Corresponding author.
E-mail address: rellie.goddard@gmail.com (R.M. Goddard).
[1] Present address: Department of Geology, Lakehead University, Thunder Bay, ON, Canada.

https://doi.org/10.1016/j.epsl.2025.119622
Received 27 May 2025; Received in revised form 15 August 2025; Accepted 3 September 2025
Available online 25 October 2025

In lieu of quantitative geobarometers, UHP metamorphism is almost exclusively identified from the preservation of coesite, a high-pressure SiO_2 polymorph. Unfortunately, coesite quickly transforms to quartz during exhumation (e.g., Mosenfelder and Bohlen, 1997; Perrillat 2003), and, as such, UHP terranes may often be overlooked. In some cases, the former presence of coesite can be inferred from parallel or radiating columnar grains of quartz assumed to have formed as quartz grows from coesite—a microstructure termed 'palisades' (e.g., Chopin, 1984; Schertl et al., 1991; Smyth, 1977). However, the identification of palisade textures is subjective, and can only be applied in cases where quartz does not undergo subsequent annealing or recrystallization.

Recently, Bidgood et al. (2021) used electron backscatter diffraction (EBSD) analysis to search for a crystallographic signature of the coesite-to-quartz transition in samples from two well-established UHP terranes: the Tso Morari Complex (NW Himalaya) and the Dora Maira Massif (Western Alps). In their work, they found that neighbouring polycrystalline domains of quartz, defined as regions with near-single-crystal orientations, had [c]-axis maxima related to one another by an ~ 90° rotation around an axis thought to align with the ⟨a⟩ direction common to both domains. Bidgood et al. (2021) attributed this crystallographic signature to the nucleation of quartz on coesite twin planes. This result provides a quantitative indicator of the former presence of coesite in felsic rocks and, thus, is a crucial and relatively simple test of deep subduction. However, whether the polymorphic quartz↔coesite transformations involve specific crystallographic relationships is highly debated within the literature, with some studies concluding that no such relationships exist (e.g., Ingrin and Golet, 1986; Langenhorst and Porter, 2002; Lenze and Stöckhert, 2007;2008; Richter et al. 2016). Before using crystallography to identify UHP terranes in nature, a better understanding of the coesite-to-quartz crystallographic signature is required.

Here, we perform EBSD analysis on natural and experimental samples to identify a crystallographic signature of the coesite-quartz transformation that emerges over a vast range of spatial and temporal scales. First, we reexamine samples from two known UHP terranes using refined and novel methodologies for exploring crystallographic relationships between parent-daughter phases. From these analyses, we redefine the signature of the coesite-to-quartz transformation and provide a physical explanation for its occurrence. We then describe a series of experiments designed to test the ubiquity of this crystallographic signature over a variety of pressure-temperature-time (*P-T-t*) paths and starting coesite microstructures. Overall, this study confirms the value of quantitative microstructural analysis for identifying UHP conditions, even in the absence of coesite in the observable mineral assemblage.

2. Geological background of natural samples

We include three natural samples in this study. First, we reanalyse samples DW09–53 and a05–10 from Bidgood et al. (2021). Sample DW09–53 is a pyrope-phengite-quartz schist from the Brossasco-Isasca unit in the Dora Maira Massif, Western Alps, where peak-pressure conditions reached ~ 35–42 kbar (3.5–4.2 GPa) and 730–830°C (e.g., Chopin and Schertl, 1999). Coesite occurs as inclusions within poikiloblastic garnets and is often surrounded by palisade quartz, making it ideal for exploring crystallographic relationships formed during the coesite-to-quartz transition. Sample a05–10 is an undeformed metagranite from a locally derived boulder within the Polokongka La region in the central part of the Tso Morari complex, on the northern margin of the Indian plate (Bidgood et al. 2021; 2024). Thermobarmetric estimates from mafic eclogite boudins suggest the Tso Morari Nappe reached UHP conditions of > 27 kbar (2.7 GPa) and ~ 640°C (St-Onge et al., 2013), though exact *P-T* conditions of the sampled boulder are unknown (e.g., O'Brien et al. 2001). In this sample we reanalyse a palisade-bearing matrix. For a full petrological description of both samples, see Bidgood et al. (2021).

One new natural sample, GSL-18-RG-011, is also included in this study. GSL-18-RG-11 is a granodiorite from the Great Slave Lake shear zone, a Paleoproterozoic continental transcurrent boundary that separates the Archean Slave and Rae cratons in the Northwest Territories, Canada (Cutts et al. 2024; Šilerová et al., 2023). Phase equilibria modelling suggests peak pressures and temperatures of ~ 11 kbar (1.1 GPa) and ~ 760°C, respectively, (Cutts and Dyck 2022; Dyck et al., 2020), comfortably within the quartz stability field. GSL-18-RG-011 therefore provides a 'null' test case for our proposed crystallographic signature.

3. Methods

3.1. Experimental procedure

To examine the coesite-quartz transformation under controlled conditions, we conducted experiments using a Deformation-DIA (D-DIA) apparatus (Figure S1; Wang et al., 2003) situated at beamline 6-BM-B of the Advanced Photon Source synchrotron, Argonne National Laboratory, Illinois, USA. Energy-dispersive X-ray diffraction was used to make *in-situ* measurements of the horizontal stress (roughly equivalent to the confining pressure) and the differential stress. In addition, X-ray diffraction enabled the *in-situ* identification of coesite and quartz (e.g., Cross et al., 2025), ensuring that samples fully transitioned between the different phases during each experiment.

It was not possible to measure stress directly from the SiO_2 sample due to weakening of the SiO_2 XRD spectra during the coesite-quartz transformation. Instead, a fine-grained olivine aggregate was included in all experiments and stacked in series with quartz to act as a stress sensor. Pressure and differential stress were calculated from the *d*-spacing of crystallographic planes within the olivine. Throughout each experiment, we varied pressure and temperature to move between the quartz and the coesite stability fields. Pressure was changed by advancing and retracting six hydraulically loaded anvils, while temperature was controlled by passing an electrical current through a graphite resistive heater. Further details on the experimental set up and procedure are summarised in Supplementary Text S1.

To compliment and expand upon the *P-T-t* paths of our natural samples, we designed two experimental pathways, hereafter referred to as Path 1 and Path 2, which are displayed schematically in Fig. 1.

Path 1 aimed to recreate the coesite-quartz crystallographic signature under the simplest experimental conditions. We started with a single crystal of Brazilian quartz, cored perpendicular to its [c] axis and normal to an {m} plane. We then placed the quartz crystal under sufficient pressure and temperature to transform it into coesite, keeping the experiment under nominally hydrostatic conditions to avoid complications related to deformation. Finally, we took the sample from the coesite stability field to the α-quartz stability field by decreasing the pressure while holding temperature constant at ~ 600°C. By transitioning from coesite to quartz at relatively low temperatures, we prevented any possible complications introduced by the transformation from high-temperature (hexagonal) β-quartz to low-temperature (trigonal) α-quartz, which is known to create Dauphiné twins defined by a 180° (equivalent to 60°) rotation around the [c] axis (Frondel, 1945). Two experiments followed Path 1: San465, which was quenched in the coesite stability field to characterise the starting microstructure for the coesite-to-quartz transition, and San466, which was quenched at the end of the *P-T-t* path in the α-quartz stability field.

In Path 2, we aimed to explore whether more complicated *P-T-t* paths could affect the occurrence or form of the crystallographic signature. Rather than single crystals, experiments on Path 2 started with a polycrystalline quartz aggregate, hot pressed from crushed and sieved particles of Black Hills quartzite. In using an aggregate, the coesite grown during the experiment is likely to have a smaller starting grain size and hence a greater density of grain-boundary nucleation sites. As in Path 1, we induced the quartz↔coesite transformations under nominally hydrostatic conditions. However, to see whether deformation affects the

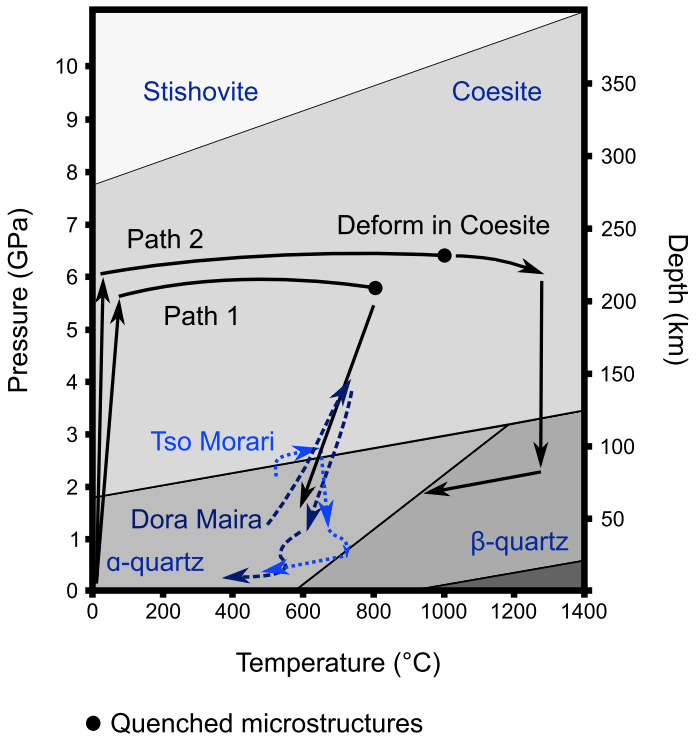

Fig. 1. Schematic pressure-temperature (*P-T*) paths of our experimental and UHP natural samples overlain on a SiO_2 phase diagram. For each experimental path, a sample was quenched within the coesite stability field (black circle) to provide a reference 'starting microstructure' for the coesite-to-quartz transition. Approximate *P-T* paths for the Dora Maira Massif and the Tso Morari complex are based on Castelli et al., (2007) and St-Onge et al. (2013), respectively. Depths were calculated assuming a density of 2830 kg·m^{-3} for the continental crust and gravitational acceleration of 9.8 m·s^{-2}.

inherited crystallography, we deformed the Path 2 samples to ~ 35 % shortening strain within the coesite field. We then took the samples from the coesite stability field to the β-quartz stability field. To test whether the transition from high-symmetry to low-symmetry quartz overprints any signature inherited from coesite, we subsequently took the sample to the β- to α-quartz phase boundary. Two experiments followed Path 2: San420, quenched in the coesite stability field after deformation to 33 % strain, and San446, quenched at the end of the *P-T-t* path at the α-β quartz phase boundary. Experiment details are summarized in Table 1.

3.2. EBSD data collection

All samples were cut and polished for EBSD analysis. For natural samples, EBSD data were collected under low-vacuum conditions (50 Pa, H_2O) on a FEI Quanta scanning electron microscope equipped with an Oxford Instruments NordlysNano EBSD camera at the University of Oxford. For experimental samples, EBSD data were collected under high-vacuum conditions using a Zeiss Supra 40 VP field-emission scanning electron microscope equipped with an Oxford Instruments Symmetry S1 EBSD detector at the Marine Biological Laboratory, Woods Hole. In all systems, samples were tilted to 70° and mapped at an accelerating voltage of 30 kV, with a step size of 0.7–18.7 μm for natural samples and 0.5–1.0 μm for experimental samples (see Table S1 in the Supplementary Material for EBSD details).

3.3. EBSD data treatment and analysis

EBSD data were cleaned and corrected for misindexing (see Supplementary Text S1) using Oxford Instruments' AZtecCrystal software and the open-source MTEX toolbox (version 5.7) for MATLAB® (e.g., Bachmann et al., 2010; Mainprice et al., 2015; Nolze and Hielscher, 2016). Grain boundaries were defined as having a misorientation ≥ 15° (Shigematsu et al., 2006) to ensure that no low-angle boundaries were included in our analysis.

Pole figures were constructed using a lower-hemisphere, equal-area projection, and a kernel halfwidth of 7.5°. For experimental samples, pole figures were constructed using the mean orientation of each grain. For natural samples, where the number of grains was limited, the one-point-per-grain data were still used, however, pole figures were weighted by the number of pixels per grain. Dauphiné twins were not

Table 1
Starting materials, experimental pathways, and quenched microstructures for D-DIA experiments.

Experiment	Path	Polycrystalline olivine stress sensor	SiO_2 sample	Deformed in coesite	β- to α- quartz transition	Qz Starting grain size[a] (μm)	Original crystal orientation	Quenched phase
San465	1	PI-2056	Single crystal	No	No	N/A	Perpendicular to [0001], normal to an $\{1\bar{1}00\}$	coesite
San466	1	PI-2056	Single crystal	No	No	N/A	Perpendicular to [0001], normal to an $\{1\bar{1}00\}$	α-quartz
San420	2	PI-1523	polycrystalline aggregate	Yes	No	4.5	N/A	coesite
San446	2	PT-1166	polycrystalline aggregate	Yes	Yes	4.5	N/A	α-quartz

[a] The arithmetic mean grain size, measured using the line-intercept method. Dauphiné twins were not removed prior to measuring intercept lengths.

removed or corrected for when constructing pole figures. As Dauphiné twinning does not change the orientation of quartz [c] axes, and instead merely rotates the ⟨a⟩ and ⟨m⟩ axes onto their symmetric equivalents, their presence should have no effect on the microstructural signatures identified in this study (e.g., Supplementary Figure S2). To measure the strength of crystal preferred orientations (CPOs), where relevant, we calculated the M-index (Skemer et al., 2005) from the full dataset of quartz orientations.

Following Bidgood et al. (2021), we used MTEX to identify and isolate quartz grains possessing the most common ('modal') orientations. As the crystallographic signature identified by Bidgood et al. (2021) depends solely on the relative orientation of [c] axes in neighbouring regions, we select maxima from spherical density functions constructed using only the [c]-axis directions. The modal [c]-axis orientations were identified using the MTEX function '*max*', which calculates the *n* pointwise maxima of spherical functions. In each case, five

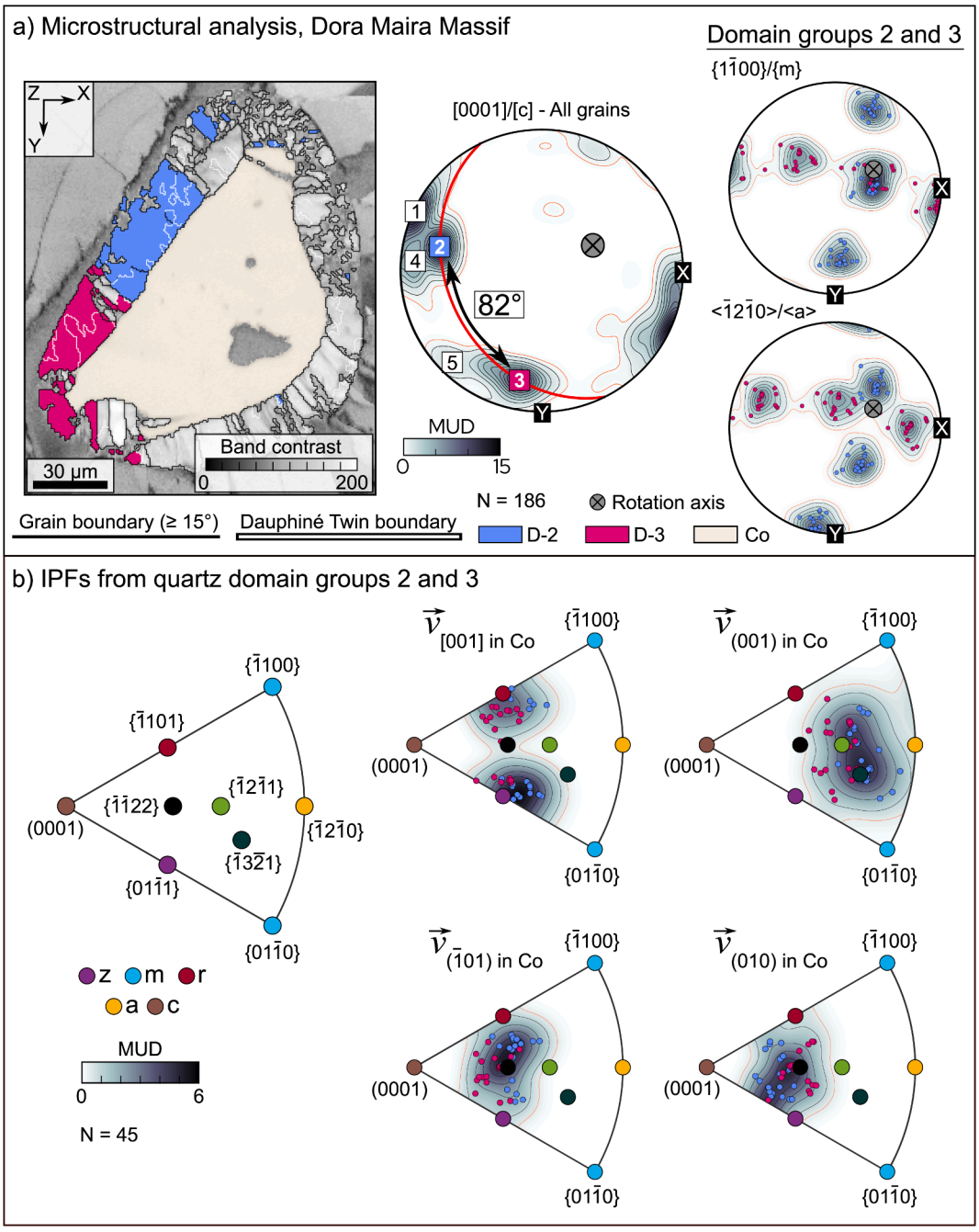

Fig. 2. Reanalysis of a Dora Maira Quartzite first presented in Bidgood et al. (2021). a) Left, band contrast map, overlain with grains belonging to [c]-axis domains D-2 and D-3; middle, quartz [c]-axis pole figure with the five most common [c]-axis orientations labelled; right, {m} and <a> pole figures for quartz grains belonging to [c]-axis domains D-2 and D-3. b) Inverse pole figures (IPFs) constructed only using grains in domains D-2 and D-3. The reference direction for each IPF is a vector corresponding to a specific crystal orientation in the parent coesite. Where relevant, contour plots represent all plotted grains, while individual mean orientations of each grain are overlain and colour coded by domain. Pole figures are presented as lower-hemisphere projections, while inverse pole figures are upper-hemisphere projections. Both pole and inverse pole figures are constructed using a contouring half-width of 7.5° and one (mean) orientation per grain weighted by the grain area. For each pole figure "N" denotes the number of grains used for its construction, where "N" has not been corrected for Dauphiné twinning. MUD stands for multiples of uniform distribution. Each contour represents a step of 1, starting at an MUD of 1, with an additional MUD of 0.5 displayed in red. For the full IPF dataset see Supplementary Figure S4.

modal orientations were identified; five maxima best describe the spherical density function for our initial Dora Maira quartzite, while keeping a consistent number of maxima throughout the study enables us to compare the frequency of any identified signature. In application, '*n*' should be set to the number of visible maxima present in the [c]-axis pole figure for quartz. Grains with [c]-axis orientations within 15° of each maximum were isolated and grouped into single regions or 'domains', hereafter denoted by the shorthand 'D-*n*' (e.g., D-1, D-2, etc.). This subsetting differs from Bidgood et al. (2021) where regions were isolated using the '*calcModes*' function in MTEX, which selects maxima based on the complete crystal orientation. Using the complete crystal orientation to identify modal orientations can result in multiple apparent 'maxima' for a single [c]-axis orientation due to Dauphiné twinning. In our work, modes calculated using the full crystal orientation do not directly align with the [c]-axis maximas (Supplementary Figure S3). Our method does not substantively change Bidgood et al.'s previous results (e.g., Section 4.1.1, Fig. 2), but it does identify grain populations more accurately.

4. Results

4.1. Natural samples

With our updated and more accurate methodology for identifying crystallographic relationships using EBSD we reexamine natural samples from both UHP and non-UHP terranes.

4.1.1. Dora Maira massif, Western Alps

Sample DW09–53A from the Dora Maira massif contains a single inclusion of coesite, surrounded by a polycrystalline mantle of quartz, contained within a garnet porphyroblast. As shown in Fig. 2a, the pole figure for the quartz [c] axis features a small number of distinct maxima, with three prominent peaks (MUDs > 10) and two additional weaker peaks (MUDs > 2). We therefore find the grain populations ('domains') belonging to the five modal orientations of [c]. Two of these domains, D-2 and D-3, are spatially correlated (i.e., neighbouring) and have [c] axes that are misorientated from one another by an 82° rotation around the pole to their common {m} plane. This specific misorientation relationship is herein referred to as our 'crystallographic signature'. It should be noted that the rotation axis in our crystallographic signature differs from the original work by Bidgood et al. (2021) who found the rotation axis to be an ⟨a⟩ axis.

As sample DW09–53A contains both the parent coesite and daughter quartz, it provides an opportunity to explore specific growth relationships in the SiO_2 system. To identify planes and directions of coincidence between the two phases, we plot inverse pole figures using reference vectors that correspond to crystallographic orientations of interest in the parent coesite, rather than using the standard, Cartesian (IPF-x, IPF-y, IPF-z) reference directions. We include in our analysis the coesite planes $(\bar{1}01)$ (see Fig. 2b) and (021) (see Figure S4), which are the twin planes that Bidgood et al. (2021) postulated could serve as nucleation sites for quartz. We explore crystallographic relationships between the original coesite crystal and both the full dataset of quartz grains and just the two neighbouring domains that are related by 82°. A complete set of IPFs can be found in Supplementary Figure S4, while select orientations are presented in Fig. 2b.

None of the crystallographic relationships previously reported in the literature (Table 2; Bidgood et al., 2021) are present within our dataset, both when considering the full dataset of quartz and just the domains exhibiting the crystallographic signature. However, some new potential relationships can be identified. For example, when considering just those grains belonging to domains D-2 and D-3, the {r} and {z} planes in quartz tend to grow along the [001] direction in coesite, the $\{1\bar{3}21\}$ family of quartz planes align with the (001) plane in coesite, and the $\{11\bar{2}2\}$ family of planes in quartz align with both the (010) and $(\bar{1}01)$ planes in coesite.

4.1.2. Polokongka granite, Tso Morari complex, Himalaya

EBSD data from the Polokongka granite are presented in Fig. 3. Individual quartz grains within the matrix are elongated and match the description of a 'palisade' microstructure. The five modal [c]-axis orientations are identified in Fig. 3a, while Fig. 3b presents the misorientation angle between each pair of [c]-axis maxima. The grains lying within 15° of these five maxima are identified in Fig. 3c. Out of the ten possible combinations of [c]-axis maxima, five are related to one another by an 81–87° rotation. Two of those [c]-axis pairs—1 & 5 and 1 & 2—are related to each other by a rotation around a pole to a shared {m} plane (Fig. 3d), similar to the crystallographic signature found in the Dora Maira sample. Spatially correlated grains within these two group sets are outlined in Fig. 3c (domains D-1 and D-5 in solid boxes, domains D-1 and D-2 in dashed boxes).

For two additional [c]-axis pairs, the rotation axis appears to more closely correspond to the ⟨a⟩ axis common to both domains (see Supplementary Figure S5), as described by Bidgood et al. (2021). For example, domains D-3 and D-4 have [c] axes related to each other by 82° around a shared ⟨a⟩ axis. This domain pairing includes the neighbouring palisade grains (see Fig. 3c) first identified as Area 1′ in Bidgood et al. (2021). However, when looking at individual neighbouring grains within these domain pairs, examples also exist where grains have a common or near-common {m} plane (e.g., domains D-1 and D-3 in areas 6 and 7 of Supplementary Figure S6).

4.1.3. Granodiorite, Great Slave Lake shear zone, Northwest Territories, Canada

For comparison, we search for the same crystallographic signature in one sample from the Great Slave Lake shear zone, which is known to have not experienced UHP conditions (Cutts and Dyck 2022; Dyck et al., 2020). Again, we find that the [c]-axis pole figure has five clear maxima. However, as can be seen in Supplementary Table S2 and Figure S7, the misorientations between pairs of [c] axes are consistently lower (25°–76°) than either that found in the Dora Maira Massif (82°) or those found in the Tso Morari complex (81°–87°).

4.2. Experiments

Having reanalysed natural samples, we now look for similar microstructures in experiments with two well constrained *P-T-t* paths.

4.2.1. Path 1: quartz single crystals

Orientation maps for the two Path 1 experiments (San465 and San466) are presented in Figs. 4a and 4b, while pressure-temperature plots are provided in Supplementary Figure S8. Experiment San465, which was quenched in the coesite stability field, contains over 3000 grains in various orientations. Newly formed coesite grains have tabular habits (Fig. 4a), like those found in other experimental studies (e.g., Mosenfelder and Bohlen, 1997; Richter et al. 2016) and in nature (e.g., Campanale et al., 2021).

Experiment San466, quenched in the α-quartz stability field, contains approximately 10,000 grains falling broadly into two populations: 1) small equant grains, and 2) larger internally distorted grains with lobate boundaries. Palisade structures and Dauphiné twins are noticeably absent. The sample contains large quartz domains composed of hundreds of grains with broadly the same [c]-axis orientations (within 15°). The five modal [c]-axis orientations are identified and labelled on the pole figure in Fig. 4d. Four out of the ten possible modal-orientation pairs have [c] axes that are related to each other by an 83°–88° rotation around the pole to a common {m} plane, similar to the crystallographic signature seen in natural samples (See Table S2). Of these four pairs, one corresponds to a pair of domains that are directly adjacent to one another (see D-1 and D-3 in Fig. 4c). The combined area of these two domains is significantly greater than the coesite grain size observed in San465. For example, the largest coesite crystal covers an area of 13,969 μm^2, whereas domains D-1 and

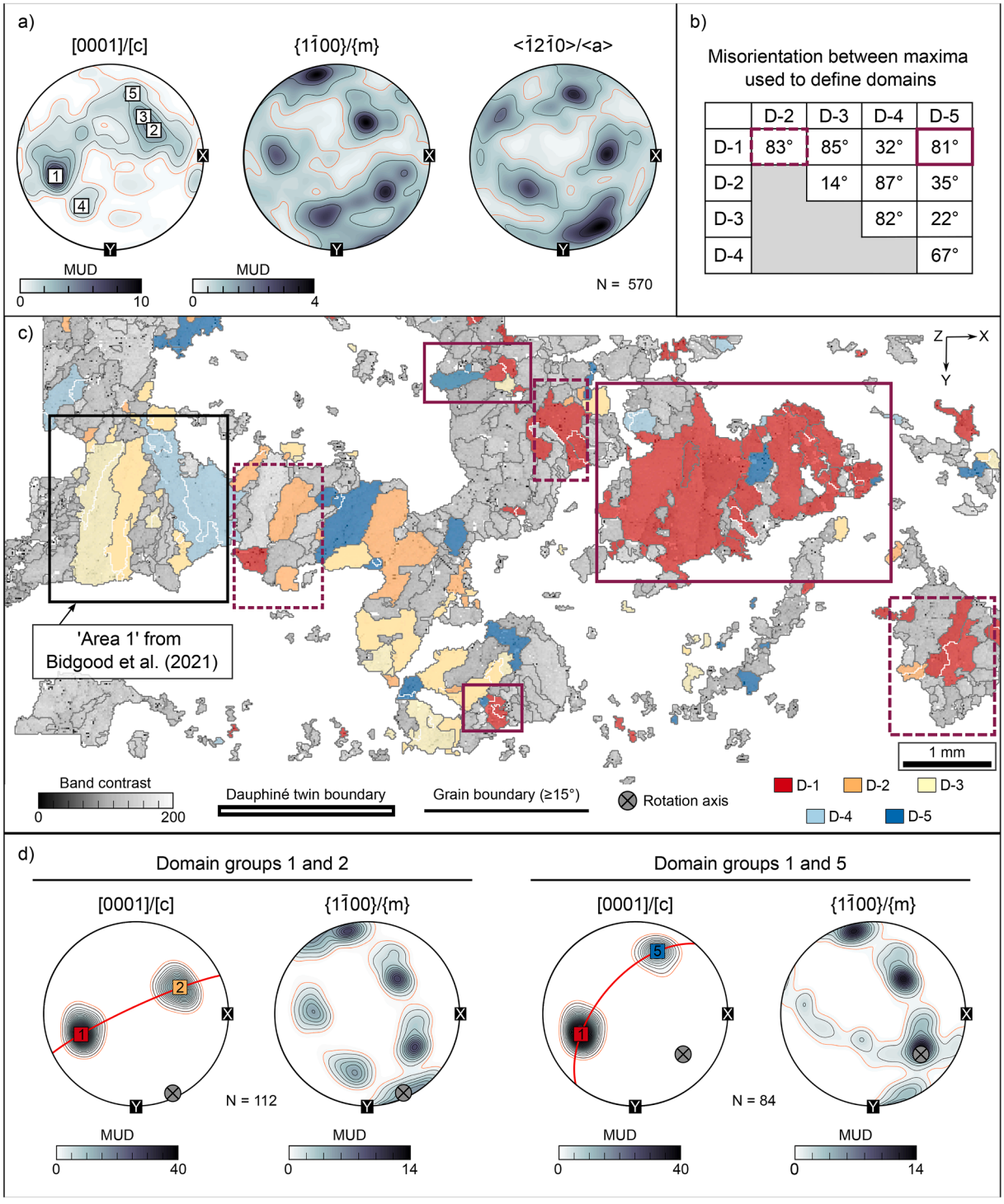

Fig. 3. Microstructural analysis of the Polokongka La region in the central part of the Tso Morari complex. a) Quartz pole figures containing all grain orientations with the five most common orientations of [c] labelled on the corresponding pole figure. b) Table insert with all the possible calculated angles of misorientation between the five [c]-axis maxima. c) Band contrast map overlain with grains that are within 15° of the five most common orientations of [c]. Purple solid and dashed boxes identify grains that have relationships indicated in table insert from (b). d) [c]-axis domain pairs that display the crystallographic signature. Pole figures were constructed as lower-hemisphere projections, using a half width of 7.5° and one (mean) orientation per grain weighted by the grain area. For each pole figure "N" denotes the number of grains used for its construction, where "N" has not been corrected for Dauphiné twinning. Contours are in steps in multiple uniform distributions (MUDs) of 1 starting from 1 (black) with an additional 0.5 MUD contour in red.

D-3 cover areas of 37,457 μm^2 and 36,359 μm^2, respectively. The other three [c]-axis pairs either cover a much smaller area (D-1/D-2 and D-2/D-4) or do not share a clear boundary (D-3/D-4, see Supplementary Figure S9).

4.2.2. *Path 2: quartz aggregates*

Microstructural analyses of the two Path 2 experiments (San420 and San446) are presented in Fig. 5, while mechanical data can be found in Supplementary Figure S8. In experiment San420, equant grains with low amounts of crystal distortion neighbour larger elongate internally

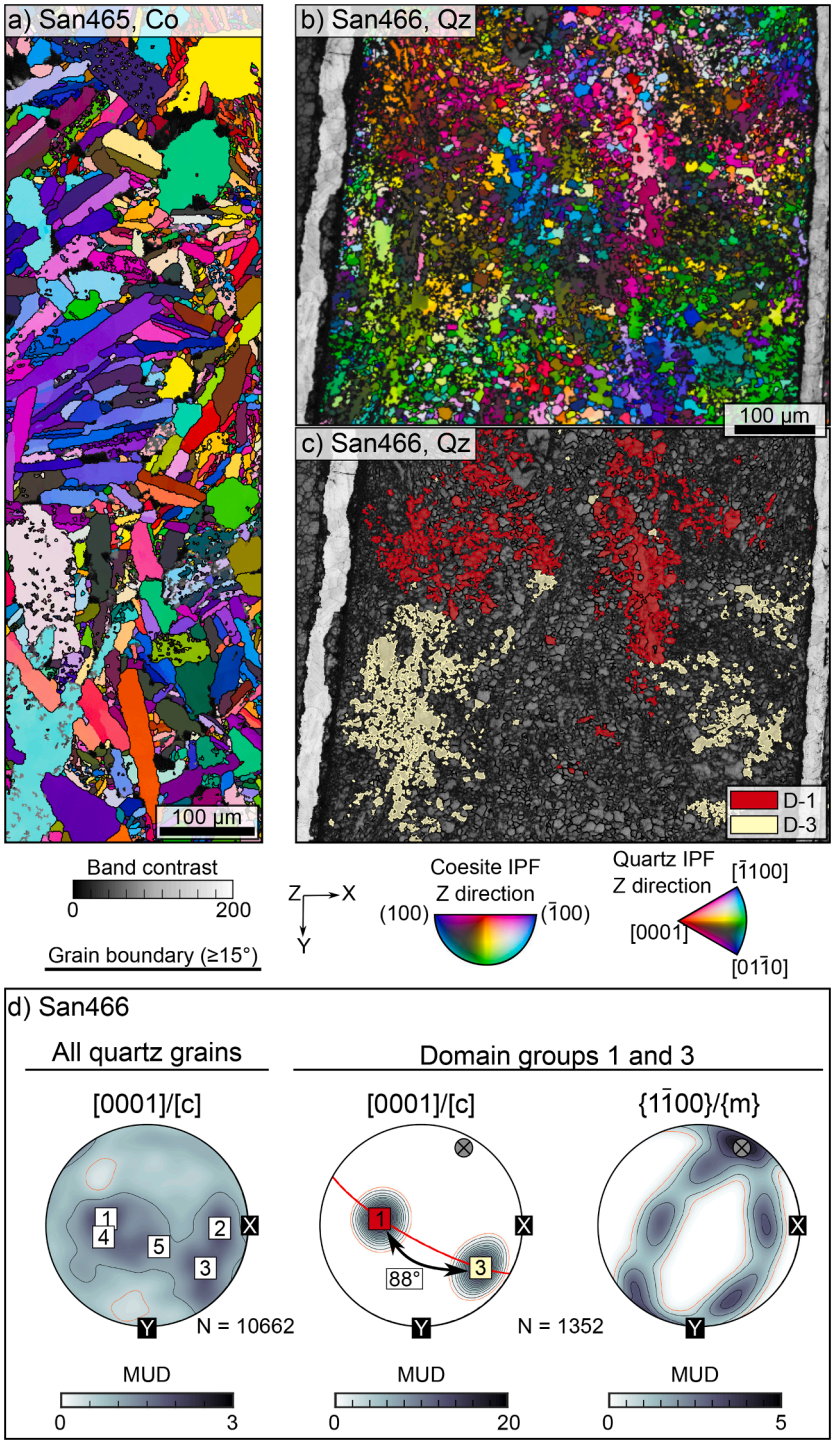

Fig. 4. EBSD data from experiments conducted on single crystals of quartz (See Figure 1, Experimental Path 1). a) Orientation map from experiment San465, quenched in the coesite stability field overlain on a band contrast map, b) Orientation map of quartz from experiment San466, overlain on a band contrast map, c) Band contrast map of b) overlain with grains within 15° of the first and third modal [c]-axis orientations, and d) Quartz pole figures containing all orientations (left) with the five modal [c]-axis orientations labelled and (right) two domains (D-1 and D-3) that correlate to neighbouring regions with [c] axes related by an 88° rotation around the pole to the common {m} plane. MUD stands for multiples of uniform distribution. All pole figures were constructed using a lower-hemisphere projection, one (mean) orientation per grain, a half width of 7.5°, and are contoured in steps in MUD of 1 starting from 1, with an additional MUD contour at 0.5 plotted in red. For each pole figure "N" denotes the number of grains used for its construction, where "N" has not been corrected for Dauphiné twinning.

distorted relict grains (Fig. 5a). Despite deformation, the coesite has a relatively weak fabric (see Supplementary Figure S10 for pole figures), with an M-index of just 0.0184 (for context a random population of orientations would give $M = 0$ whereas a single crystal would give $M = 1$; Skemer et al., 2005).

In Experiment San446, quenched at the α-quartz, β-quartz boundary, the microstructure once again contains domains consisting of hundreds of quartz grains with broadly the same [c]-axis orientations. The five modal orientations are identified and labelled on the pole figure in Fig. 5d. Of the five maxima, one out of ten possible pair combinations

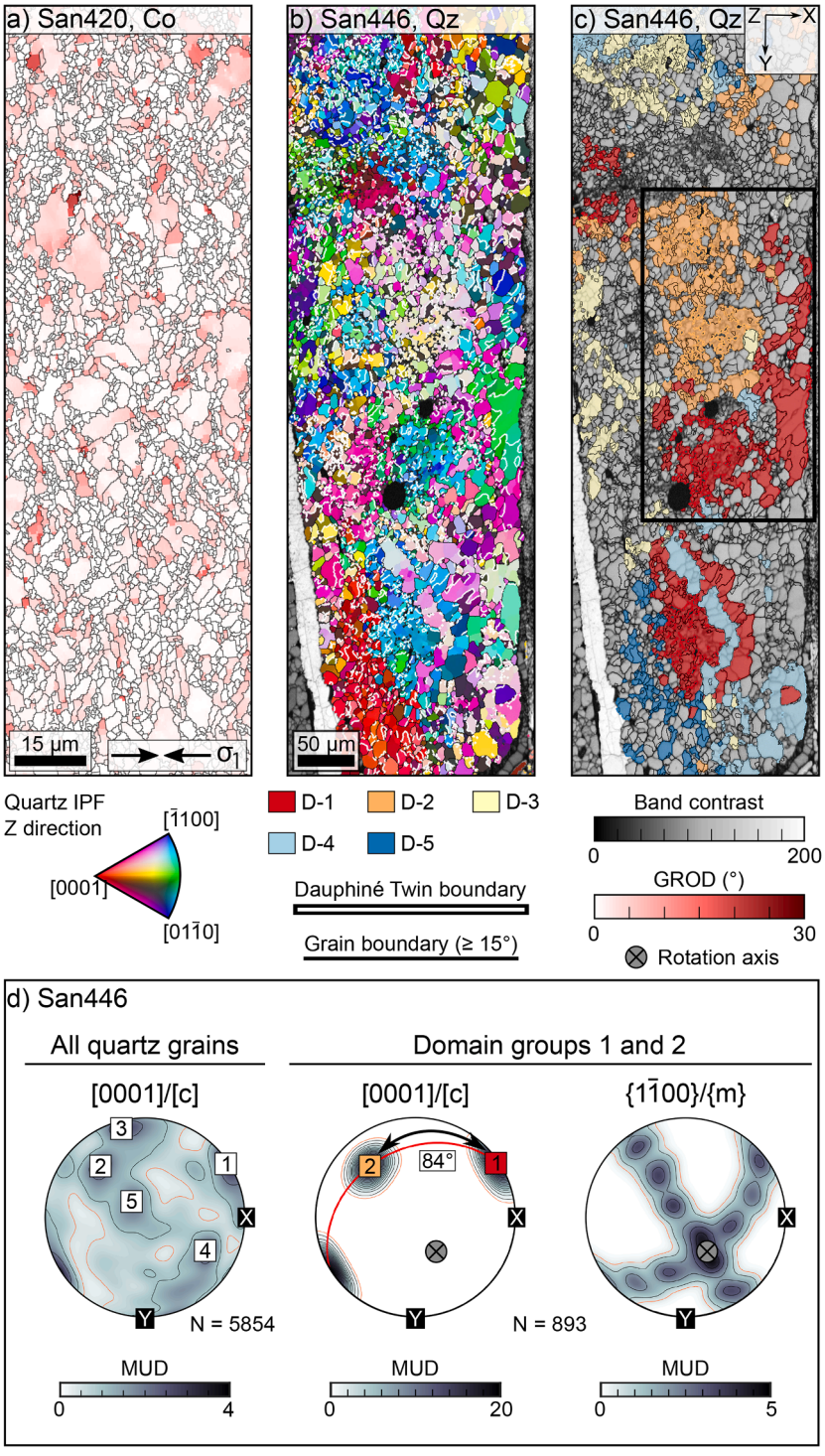

Fig. 5. EBSD data from experiments conducted on quartz aggregates (see Figure 1, Experimental Path 2). a) Grain Reference Orientation Deviation (GROD), that is, the misorientation of each pixel related to the mean grain orientation, for coesite from Experiment San420. b) Crystal orientations overlain on band contrast data from Experiment San446, which was quenched in the α-quartz stability field after first being deformed in the coesite stability field and taken hydrostatically through the coesite to β-quartz, then β-quartz to α-quartz phase transformations. In addition to grain boundaries, Dauphiné twins are plotted in white. c) Band contrast map overlain with grains within 15° of the five-most common orientations of [c] in quartz. The black box indicates neighbouring regions that show an 84° rotation of the [c] axis around the pole to the common {m} plane. d) Pole figures constructed from EBSD data of experiment San446, using all quartz grains (left) and just those grains within 15° of the first and second most common [c]-axis maxima. MUD stands for multiples of uniform distribution. Pole figures are lower-hemisphere projections, were constructed using one (mean) orientation per grain, a half width of 7.5°, and are contoured in steps of MUD of 1 starting from 1, with an additional MUD contour at 0.5 plotted in red. For each pole figure "N" denotes the number of grains used for its construction, where "N" has not been corrected for Dauphiné twinning.

have [c] axes that are related to each other by the same crystallographic signature that we see in the natural samples and in the single-crystal experiment (Supplementary Table S2). Grains belonging to this domain pair (D-1/D-2) are spatially correlated and have [c] axes that can be related by a rotation of 84° around the pole to the common {m} plane (Fig. 5c). Again, the combined area of these two domains is significantly larger than the expected starting grain size in coesite; the largest coesite crystal in San420 covers an area of 648 μm^2, whereas domains D-1 and D-2 cover areas of 21,630 μm^2 and 17,094 μm^2, respectively.

5. Discussion

5.1. Japan twins: A crystallographic signature for the coesite-to-quartz transition

Bidgood et al. (2021) identified a microstructural signature in quartz for the coesite-to-quartz transition, which enables the identification of UHP terranes via EBSD analysis. Neighbouring quartz domains, defined as regions with orientations approximating a single crystal, were described to have [c]-axis maxima related to one another by a misorientation of ~ 90° around the ⟨a⟩ axis common to both domains. However, in the Bidgood et al. (2021) study, misorientation axes and angles were visually estimated from pole figures rather than measured precisely. Using MTEX, we find that spatially correlated domains in the Dora Maira quartzite and the Polokongka granite commonly have [c] axes misoriented by 82°–86°. Although some neighbouring domains in the Polokongka granite are related by a rotation around the common ⟨a⟩ axis, the misorientation axis found consistently across both samples is the pole to the common {m} plane. In contrast, we find no evidence of a similar signature in sample GSL-18-RG-11, known to have only reached upper-amphibolite conditions. Our results therefore suggest that the described crystallographic signature arises from the coesite-quartz transition.

The rotation angle and axis in our crystallographic signature strongly matches that of a Japan twin (e.g., Sunagawa et al., 2004), also known as a Verespatak twin (e.g., Lenart et al., 2012). Traditionally, Japan twins are classified as a growth twin on the {11$\bar{2}$2} face in quartz that places two [c] axes ~ 85° apart through a rotation around the pole to the {m} plane common to both twins (see Fig. 6a for schematic illustration). However, in nature, Japan twins tend to be found in mineral veins (e.g., Yasuda and Sunagawa, 1982) and have subhedral or euhedral crystal habits (e.g., Sunagawa et al., 2004; White, 2014). While some studies have associated Japan twinning with deformation (Bestmann et al.,

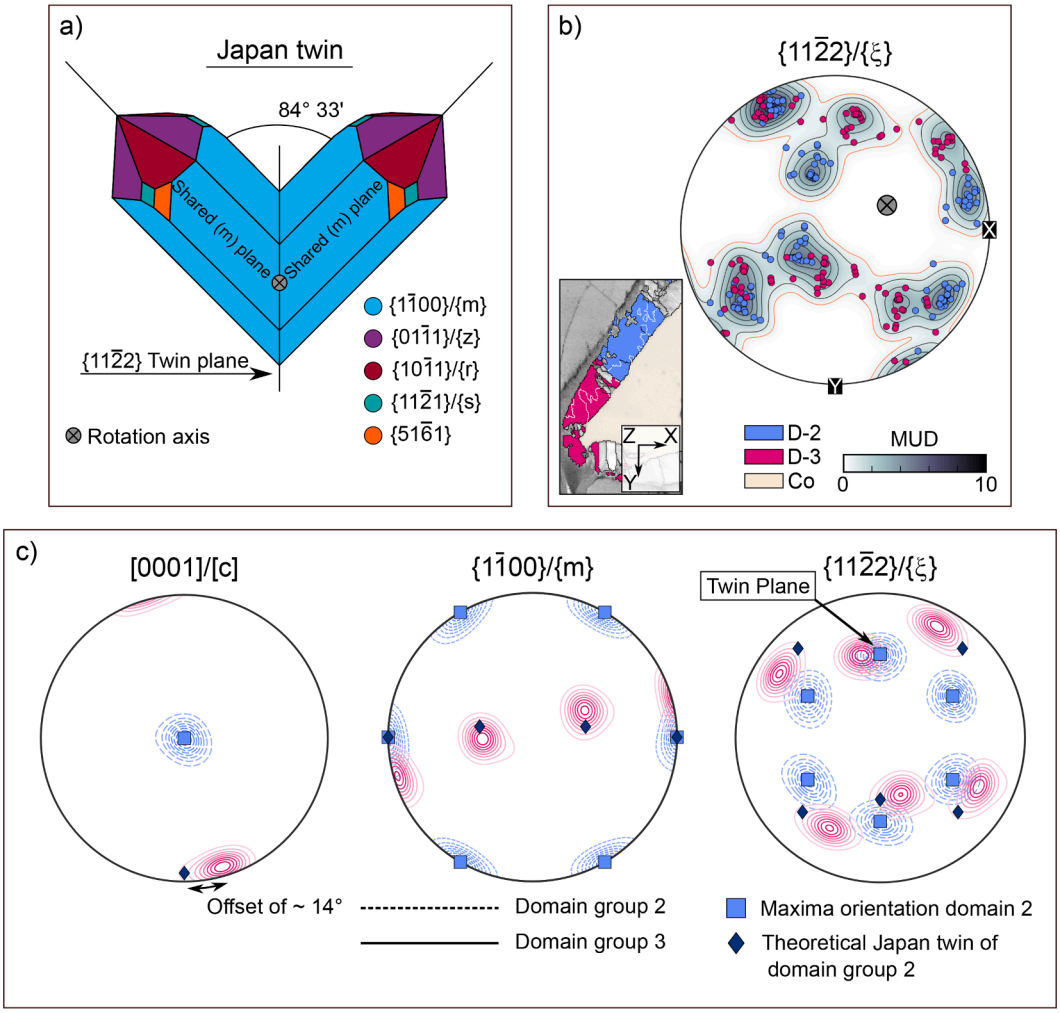

Fig. 6. Identification of a Japan twin within the Dora Maira Quartzite, Western Alps. a) Japan twin schematic. b) Pole figure of the Japan twin plane in quartz constructed with grains belonging to domains D-2 and D-3. Insert shows a portion of the band contrast map, originally plotted in Figure 2, overlaid with grains corresponding to domains D-2 and D-3. c) Comparison between a theoretical Japan twin of domain D-2 (blue diamonds) and the actual orientation of domain D-3 (solid pink contours). Both datasets have been rotated into the domain D-2 reference frame. Pole figures are constructed using a half-width of 7.5° and one (mean) orientation per grain, weighted by the grain area. MUD stands for multiples of uniform distribution. Each contour represents a step of 1, starting at an MUD of 1, with an additional MUD of 0.5 displayed in (b) in red.

2021), Japan twins have never been described as a transformation twin or associated with UHP conditions to our knowledge.

To test that our crystallographic signature does, in fact, arise from Japan twinning, we compare the orientation of two neighbouring domains in the Dora Maira Quartzite—herein referred to as domains D-2 and D-3—to the theoretical Japan-twin relationship (Fig. 6c). We examine the crystallographic orientation of D-3 using pole figures constructed in the crystallographic reference frame defined by the mean orientation of D-2. This construction enables us to more easily visualise any misorientation relationships. The orientation data from domains D-2 and D-3 are contoured and plotted with dashed and solid lines, respectively. We then overlay the average orientation of domain D-2 as light blue squares and its theoretical Japan twin as dark blue diamonds. This theoretical twin can then be compared to orientations in domain D-3. As can be seen in Fig. 6c, our data broadly match the theoretical twin, but are offset by 14°. As the discrepancy between our data and the theoretical solution can be explained by the internal distortion within the quartz grains (see grain orientation spread map in Supplementary Figure S11), we consider the analysis to support the presence of a Japan twin relationship in the Dora Maira Massif.

5.2. Epitaxial nucleation of Japan twins during the coesite-to-quartz transition

Having identified our crystallographic signature as a Japan twin, we now seek to understand why Japan twins nucleate during the coesite-to-quartz transition. As not all quartz within our samples contain Japan twins, the occurrence of these twins must be due to a preferential nucleation and growth on certain surfaces within coesite. Crystal nucleation where the orientation of the nucleating phase is governed by the orientation of a parent substrate is termed epitaxy (e.g., Poppa, 1963). To understand epitaxial nucleation in our system, we first must identify the plane of coincidence in quartz and coesite. Many alternative and conflicting epitaxial relationships for quartz and coesite have been identified within the literature using techniques such as TEM, EBSD, and X-ray diffraction (e.g., Campanale et al., 2021; Ruiz-Cruz and Galdeano, 2012; Zinn, Hinze, et al., 1997, Zinn, Lauterjung, and Wirth, 1997), a summary of which can be found in Table 2. Multiple studies have also recorded no epitaxial relationship between quartz and coesite (e.g., Ingrin and Golet, 1986; Langenhorst and Porter, 2002). While these previous studies on epitaxy have focused on bulk microstructures, our study focuses on localised quartz domains that display a crystallographic signature for the coesite-to-quartz transformation. Using the Dora Maira sample, which is preserved mid-way through the coesite-to-quartz transition, we consider just the quartz domains that feature Japan twinning. Although we see none of the previously proposed epitaxial relationships (Figure S4), we do find coincidence between the $\{11\bar{2}2\}$ quartz planes, that is, the Japan twin plane, and the (010) and $(\bar{1}01)$ planes in coesite (see Fig. 2), both of which are themselves twin planes. Nucleation of the Japan twin must therefore have occurred on one of these two planes.

Assuming that epitaxy in the coesite-quartz system results from the preferential nucleation of quartz on energetically favourable sites, then it is logical that the spacing of silica tetrahedra in the Japan twin plane of quartz would be similar to that of the nucleation plane in coesite. To compare the tetrahedral spacing within our planes of interest, we performed supercell simulations within the software Crystalmaker®. In Fig. 7, we describe the spacing between different tetrahedra units in the $\{11\bar{2}2\}$ plane, in both α- and β-quartz, and the $(\bar{1}01)$ and (010) planes in coesite.

Tetrahedra within the quartz $\{11\bar{2}2\}$ twin plane in both α- and β-quartz are periodicity arranged in two perpendicular directions (Fig. 7a), herein referred to as the horizontal and vertical directions based, for convenience, on their orientations as plotted in Fig. 7. The tetrahedral spacing is directionally dependent, with the vertical spacing being greater than the horizontal spacing. In coesite, only one direction in the $(\bar{1}01)$ plane—the vertical direction in Figure 7—has tetrahedra that have a spacing periodically similar to that found in the $\{11\bar{2}2\}$ plane in quartz, specifically the horizontal direction. In all other directions, the tetrahedra either have a very large spacing (e.g., 12.37 Å) or does not exhibit periodicity within the length-scale of the unit cell. Therefore, only one orientation of the $\{11\bar{2}2\}$ plane in quartz can favourably align tetrahedra with coesite tetrahedra in the $(\bar{1}01)$ plane. As such, one orientation of coesite could result in favourable nucleation of one orientation of quartz.

Within the (010) plane in coesite, the spacings between every T1 site within the [100] direction, and every other site within the [001] direction are very similar, at 7.14 Å and 7.17 Å, respectively. As a result, the spacing of tetrahedral units on the $\{11\bar{2}2\}$ plane in quartz is either within 2 to 4 % of coesite in the horizontal direction (7.30 Å and 7.40 Å in α- and β-quartz, respectively) or between 19 and 21 % larger than coesite in the vertical direction (8.51 Å and 8.65 Å in α- and β-quartz, respectively). The smaller spacing in quartz has therefore two energetically favourable orientations for templating on the (010) plane in coesite. Fig. 7b demonstrates that when nucleation and growth of the $\{11\bar{2}2\}$ plane in quartz occurs in these two orientations, the [c] axes of each quartz twin are ~ 85° apart, matching our crystallographic signature. The two orientations that form the Japan twin therefore can be accounted for by the nucleation and growth of energetically favourable orientations of the $\{11\bar{2}2\}$ plane in quartz on the (010) plane in coesite.

5.3. The prevalence of the crystallographic signature in UHP terranes

While our work on epitaxy in the coesite-quartz system supports the preferential growth of Japan twins on the (010) plane in coesite, it is unclear how different *P-T-t* paths or the presence of different nucleation sites affects the prevalence of this crystallographic signature. For example, while our results support previous suggestions that twin boundaries are favourable sites for nucleation (e.g. Langenhorst and Porter, 2002), other microstructures such as dislocations (e.g., Gómez-Ramírez, and Pound, 1973) and grain boundaries (e.g., Mosenfelder and Bohlen, 1997; Perrillat et al., 2003) have also been suggested

Table 2
Previously reported crystallographic relationships in the SiO_2 system.

Reference	Sample origin	Transformation	Analytical method	Coesite	Quartz
Campanale et al. (2021)	Kamil Crater, Egypt	Qz→Co	TEM	(010)	$\{10\bar{1}1\}/\{\bar{1}011\}$
Campanale et al. (2021)	Australasian tektite strewn field	Qz→Co	TEM	(010)	$\{1\bar{3}21\}/\{\bar{1}3\bar{2}1\}$
Ruiz-Cruz & Galdeano (2012)	Ceuta zone, Northern Rif, northwest Africa	Co→Qz	EBSD	(001)	(0001)
Ruiz-Cruz & Galdeano (2012)	Ceuta zone, Northern Rif, northwest Africa	Co→Qz	EBSD	(010)	$\{10\bar{1}0\}$
Zinn et al. (1997a, 1997b)	Experiment, Finely powdered quartz in a cubic-anvil apparatus	Qz→Co	X-ray diffraction	(111)	$(10\bar{1}1)$

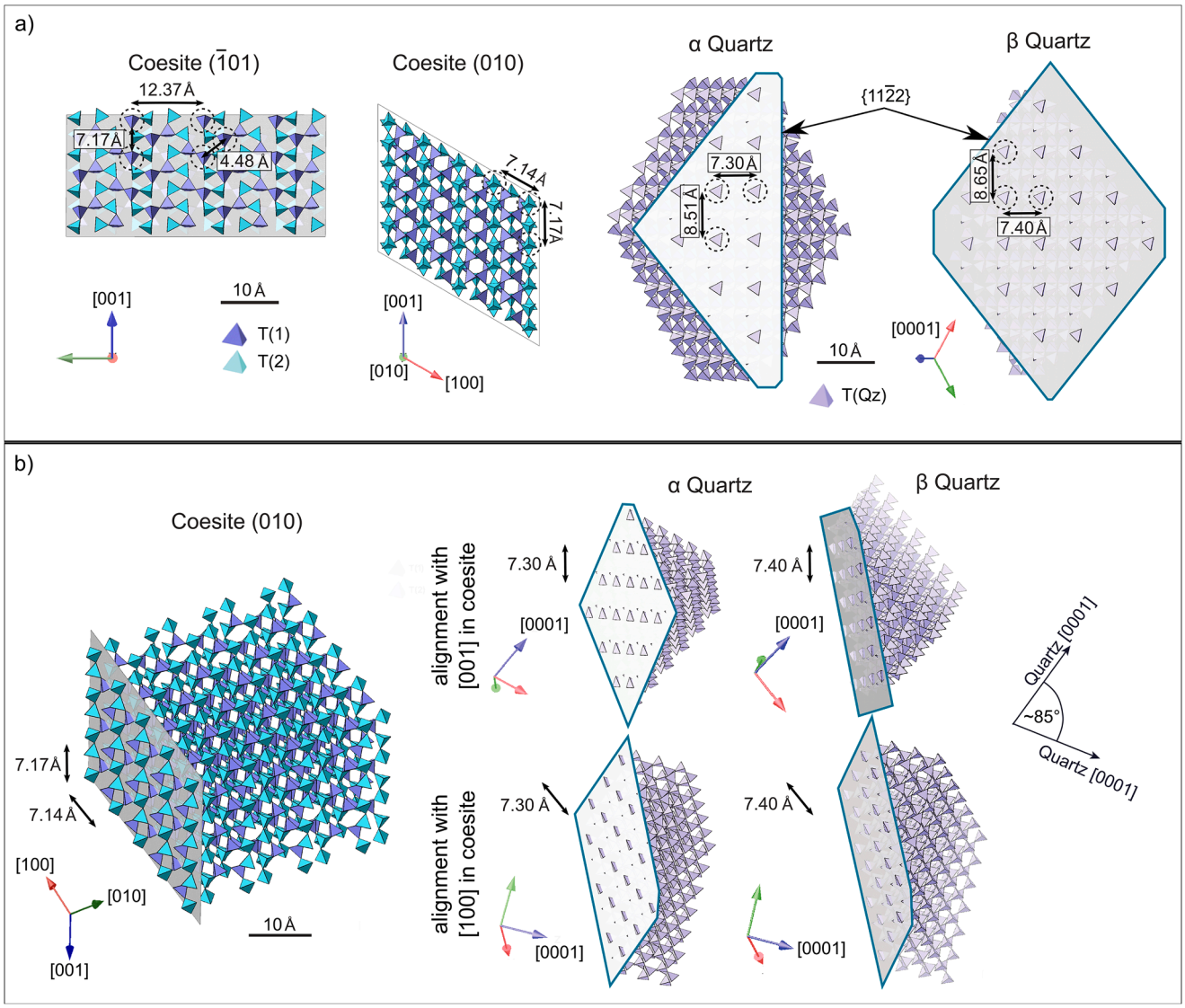

Fig. 7. Inter-tetrahedral bond length in planes of interest in coesite and quartz. a) Lattice spacing between tetrahedral units within the $(\bar{1}01)$ and (010) planes in coesite and the $\{11\bar{2}2\}$ twin plane in quartz. b) Rotation of quartz crystals into favourable nucleation orientations based on the spacing of SiO_2 tetrahedra in the $\{11\bar{2}2\}$ and (010) planes in quartz and coesite, respectively. It should be noted that in coesite the different sites, T1 and T2, are crystallographically the same, but are different sizes, and are both nominally filled by Si.

as preferential nucleation sites due to their low free energy. In addition, while undeformed samples were deliberately selected by Bidgood et al. (2021), the quartz–coesite transition has been linked with strain localisation (e.g., Asano et al., 2021) and transient weakening (e.g., Cross et al., 2025; Zhou et al., 2005). As deformation both increases the dislocation density and reduces grain size, it is necessary to test whether Japan twins also form when high concentrations of other nucleation sites exist. The *P-T-t* paths of the Dora Maira quartzite and the Polokongka granite, also only cover a small fraction of the SiO_2 *P-T* space (Fig. 1) with neither sample spending significant time in the β-quartz stability field. It is therefore of interest to ensure that *P-T-t* paths that pass from the coesite to the β-quartz stability field also produce Japan twins. In short, while the presence of Japan twins are a quantitative indicator of UHP conditions it is not yet clear if they are a ubiquitous feature of the coesite-to-quartz transition under different *P-T* paths and stress states and, as such, their absence cannot yet be used to indicate a rock that has not undergone the coesite-quartz transition. We therefore need to test for our crystallographic signature under conditions as variable as those found in nature.

We conducted a suite of experiments to test for the reported crystallographic signature under two *P-T-t* paths. As a control for whether experiments can accurately recreate natural microstructures, the first path emulates the phase transformations of the Dora Maira, that is, it passes from the coesite to the α-quartz stability field. The second path tested conditions different from our natural samples, with deformed coesite transitioning first to β-quartz and then to α-quartz. In both sets of experiments, we find neighbouring domains that have roughly single-crystal orientations (within 15°) with their [c] axes misoriented by 83°–88°, around an axis that aligns with the pole to the common {m} plane, that is, we find Japan twins. Quenched quartz microstructures from Path 1 contain three sets of Japan twins (Table S2, Figs. 4, and S9), compared to the one set identified at the end of Path 2 (Table S2, Fig. 5). Therefore, while a greater concentration of nucleation sites does not fully suppress the crystallographic signature it may limit how pervasive Japan twins are.

Interestingly, the broad 'single-crystal' domains in our experiments cover a much larger area than any coesite grain in the nominal starting microstructures. Put simply, one coesite grain does not become one

quartz Japan twin domain in our experiments. Instead, preferential nucleation of $\{11\bar{2}2\}$ in quartz on (010) in coesite is followed by rapid crystal growth, which ultimately consumes SiO_2 outside of the original grain of nucleation (See Fig. 8a).

Our interpretation that a single Japan twin could outgrow the coesite grain from which it nucleates differs from our natural samples, where quartz domains obeying the Japan twin law are not vastly larger than the purported parent coesite. One explanation for this discrepancy is the relative contribution of nucleation and growth during the phase transformation in experiments compared to those in nature. In general, experiments probing the quartz-to-coesite transformation at conditions that overstep the phase boundary are said to be dominated by growth (e.g., Nagai et al., 1997; Perrillat et al., 2003; Rubie et al., 1990; Zinn et al., 1997), meaning that nucleation is effectively instantaneous. If our experiments are controlled by growth kinetics, the differences between natural and experimental samples must relate to the relative growth rates of the quartz crystal facets at the two sets of conditions.

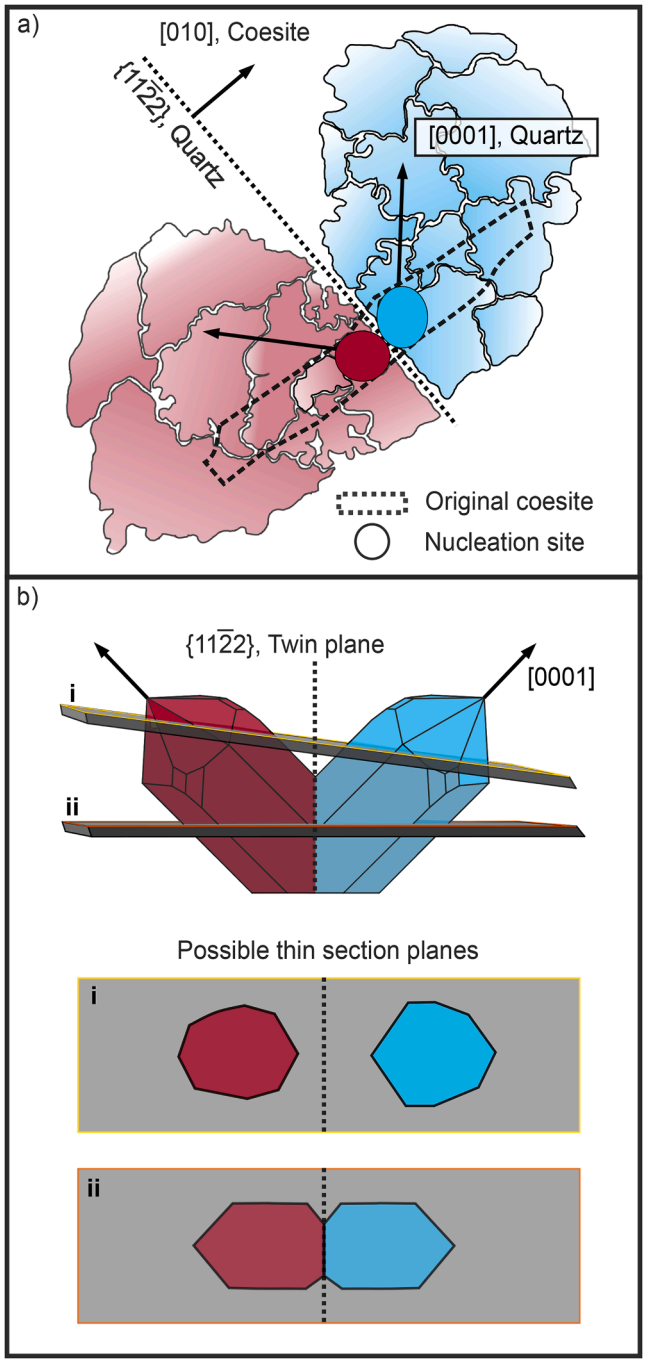

Fig. 8. Schematic illustration of the nucleation and growth of a Japan Twin. a) Quartz growing beyond the bounds of the initial coesite grain and b) Influence of the orientation of the thin section plane on the captured quartz microstructures.

Although numerous experimental studies have focused on transformation kinetics (e.g., Mosenfelder and Bohlen, 1997; Perrillat et al., 2003; Zinn et al., 1997) it is difficult to extrapolate such kinetic models to natural conditions (e.g., Rubie et al., 1990). Nevertheless, higher temperatures clearly result in faster growth rates (e.g., Perrillat et al., 2003). Assuming that nucleation was indeed instantaneous, the larger microstructural footprints of the Japan twins in our experiments compared to those in nature could result from the growth rate of Japan twins having a greater temperature dependence than other grains. However, we are unable to test this hypothesis with our current suite of experiments.

Differences in growth rates between experiments and nature may also explain the noticeable absence of traditional 'palisade' microstructures in our experimental samples, with palisade development favouring slower growth rates. For instance, Mosenfelder and Bohlen (1997), who cooled and depressurised their experiments slowly, and stayed close to the quartz-to-coesite transition, identified palisade textures in their samples. In contrast, we largely overstepped the phase boundary, resulting in rapid transformation rates and an absence of palisade microstructures. Conveniently the presence of Japan twins in the absence of palisade microstructures indicates that the latter is not the sole diagnostic feature of the coesite-quartz transition, making our crystallographic method of identifying UHP terranes applicable even in the absence of palisade quartz.

Our experimental results have two further discrepancies from natural samples that need to be discussed. First, the two domains that constitute the Japan twin do not always share a clear boundary. However, as demonstrated by (i) in Fig. 8b, the lack of a twin boundary within our EBSD maps can easily be explained by a stereological effect, with the nucleating interface being out of the thin-section plane. Second, the two domains that comprise the Japan twin consist of numerous grains with orientations approximating a 'single-crystal'. It is possible these grain boundaries result from static recrystallisation of originally large quartz grains (i.e., true single crystals), driven by dislocations generated during growth (e.g., Lathe et al., 2005). Such "growth dislocations" can result from inhomogeneous temperature fields, rapid crystallisation, or due to any slight variation in the stress field away from hydrostatic conditions, all of which are common features of D-DIA experiments. Although growth dislocations and subsequent low-angle boundaries are likely to also occur in nature, prolonged time at high temperatures prior to or during exhumation would allow for recovery and annealing processes to remove such microstructures (e.g., Lenze et al., 2005).

Microstructural evidence of Japan twins in both experimental and natural samples provide a definitive link between the two environments, indicating the mechanism for the coesite-to-quartz transitions remains consistent across a broad spectrum of conditions.

5.4. *Observing our crystallographic signature in nature*

In this study we have identified a crystallographic signature for quartz-after-coesite in four rocks that had been to UHP conditions and verified its absence in one sample that did not cross the quartz-to-coesite phase boundary. To further increase confidence in our crystallographic signature, we assess the probability that the signature could be a statistical artefact of a randomly distributed fabric. We begin by creating a dataset of $\sim 10^6$ randomly oriented grains drawn from a uniform orientation distribution function. We then compare the relative orientations of [c] axes, {m} planes, and $\{11\bar{2}2\}$ twin planes to those

generated by a reference orientation defined as having Euler angles of 0°, 0°, 0°. We consider the comparison to satisfy our crystallographic signature when it has [c] axes that are 85° (within 5°) apart, a common {m} plane (within 15°) and a common $\{11\bar{2}2\}$ twin plane (within 15°). While 17 % of grain pairs have [c] axis misoriented by 85° ± 5°, only 3 % have {m}, $\{11\bar{2}2\}$, and [c] that are all in accordance with the crystallographic signature for quartz-after-coesite, an almost exact match to the number of Japan Twins identified in the starting quartz aggregate after having been pressurised and heated within the D-DIA without the phase transformation to coesite (see experiment San519, supplementary Figure S12). Note that we do not impose an additional constraint that our random, synthetic aggregate contain large domains of neighbouring grains with near-single-crystal orientations. Imposing this constraint would make it considerably less likely that the observed crystallographic signatures arises purely by chance.

While Japan Twins do occur elsewhere in nature as contact twins, they are commonly associated with hydrothermal systems in which there is little environmental disturbance (Sunagawa, 1991). With an appropriate level of sample and outcrop description, we can therefore be confident that for samples of subducted and metamorphosed continental crust, the Japan twin signature indicates nucleation from previous coesite. While identifying a greater number of Japan twin pairs will obviously increase confidence in any UHP categorisation, using additional microstructural criteria, such as the occurrence of Japan twins in garnet hosts grown at high pressure or in palisade microstructures, would further corroborate a UHP designation. In deformed rocks, the alignment of the $\{11\bar{2}2\}$ twin plane subparallel to the shear plane would also act to support the nucleation of quartz from coesite as it matches the expected orientation of the (010) plane after rigid rotation of coesite clasts (e.g. Richter et al., 2016).

Our crystallographic signatures offers an objective tool that can be applied to all felsic rocks, but as with any geothermometer/geobarometer, its effectiveness requires a holistic approach to identifying UHP terranes, which considers both the geological and microstructural context of the identified Japan Twins. In addition, quartz inclusions taken to UHP conditions within a strong host that grew on the prograde path will be shielded from the external pressure (e.g., Alvaro et al., 2020) and as such lack Japan Twins. Nevertheless, to increase the ease with which this method can be used to identify new UHP terranes, we have developed a graphical user interface for identifying the Japan twin signature using EBSD data (available at https://github.com/RellieGoddard/CrystallographicSignature.git).

6. Conclusion

Identifying continental crust that has been subducted to, and subsequently exhumed from, depths in excess of 100 km is challenging due to the poor preservation of UHP minerals such as coesite. Using EBSD data collected from both natural and experimental samples, we demonstrate a crystallographic signature of the coesite-to-quartz transition, where quartz contains adjacent domains misoriented from one another by a Japan twin relationship, that is, by an ~ 85° rotation of [c] around the pole to the common {m} plane. Using natural samples preserved midway through the coesite-to-quartz transition, and augmented by supercell simulations, we explain this growth relationship through the energetically favourable alignment of the $\{11\bar{2}2\}$ plane in quartz on the (010) twin plane in coesite. High-pressure, high-temperature experiments confirm that the crystallographic signature also arises over a vast range of *P-T-t* paths regardless of whether coesite is replaced by α-quartz or β-quartz, and regardless of the concentration of alternative nucleation sites such as dislocations or grain boundaries. Overall, this study expands our understanding of the crystallographic mechanisms involved in the coesite-to-quartz transformation and provides an objective and widely applicable new tool for identifying UHP terranes.

Data availability statement

Mechanical data from the Deformation-DIA experiments alongside EBSD data of recovered samples are available from *Figshare* and can be accessed via the link https://doi.org/10.6084/m9.figshare.29053211. An interactive toolbox for identifying the Japan Twin signature using EBSD data can be found at https://github.com/RellieGoddard/CrystallographicSignature.git.

CRediT authorship contribution statement

Goddard: Writing – review & editing, Writing – original draft, Validation, Resources, Project administration, Methodology, Investigation, Formal analysis, Data curation, Conceptualization. **Andrew J. Cross:** Writing – review & editing, Supervision, Methodology, Funding acquisition, Formal analysis, Data curation. **Geoffrey E. Lloyd:** Writing – review & editing, Methodology, Investigation, Formal analysis. **Thomas Breithaupt:** Writing – review & editing, Methodology, Investigation, Formal analysis, Data curation, Conceptualization. **Kathryn M. Kumamoto:** Writing – review & editing, Supervision, Formal analysis, Data curation, Conceptualization. **Brendan V. Dyck:** Writing – review & editing, Validation, Investigation, Formal analysis. **Haiyan Chen:** Methodology, Investigation, Formal analysis. **Andrew Parsons:** Writing – review & editing, Data curation, Conceptualization. **Anna K. Bidgood:** Writing – review & editing, Data curation, Conceptualization.

Declaration of competing interest

The authors declare that they have no known competing financial interests or personal relationships that could have appeared to influence the work reported in this paper.

Acknowledgements

Natural samples were collected during three field seasons. Sample DW09-53 was collected on the 2009 field excursion, led by Philippe Agard, funding through a joint France-UK academic exchange programme grant entitled 'The Hubert Curien Partnership (HCP) Alliance programme' awarded to P.Agard and C.-J- De Hoog. Sample a05-10 was collected on the 2017 field excursion led by Anna Bidgood, funded by the Natural Environmental Research Council, grant number NE/L002612/1. Sample GSL-18-RG-11 was collected on the 2018 field excursion to the Northwest Territories led by Rellie M. Goddard, funded by the Natural Environmental Research Council, grant number NE/L002612/1 (to R.M.G), internal funds from University College, Oxford, The Mike Coward Fund from the Geological Society (to R.M.G), and support from a Natural Science and Engineering Research Council Discovery Grant, grant number RGPIN-2019-04248 (to B.D.).

Experimental work was undertaken at the Advanced Photon Source (APS), an Office of Science User facility operated by the U.S. Department of Energy by Argonne National Laboratory. Use of the APS was supported by the U.S. Department of Energy, Office of Science, Office of Basic Energy Sciences, under Contract No. DE-AC02-06CH11357. Use of the 6-BM-B beamline was supported by COMPRES, the Consortium for Materials Properties Research in Earth Sciences, under NSF Cooperative Agreement EAR 16-06856. Portions of this work were performed under the auspices of the U.S. Department of Energy by Lawrence Livermore National Laboratory under Contract DE-AC52-07NA27344. LLNL-JRNL-2004734. Funding for materials and trips to APS was provided by NERC Environmental Research DTP grant NE/L002612/1 (to R.M.G.), the Royal Commission for the Exhibition of 1851 fellowship (to T.B.), National Science Foundation grants EAR-2003389 (to A.J.C.), EAR-2023128 (to A.J.C.), and EAR-1806791 (to K.M.K.), and UK Research and Innovation Future Leaders Fellowship grant MR/V021788/1 (supporting T.B.).

The experimental campaign was greatly supported by the scientists present at the APS during our allocated beam time, particularly Lars Hansen, Diede Hein, Adaire Nehring, Leif Tolke, and Amanda Dillman who additionally helped make assembly components and provided starting materials. Jon Wells and Matthew Beverly-Smith helped establish a thin-sectioning method and sectioned all these finicky samples under tight deadlines. EBSD collection was aided by Louie Kerr at the Marine Biological Laboratory in Woods Hole, MA.

Supplementary materials

Supplementary material associated with this article can be found, in the online version, at doi:10.1016/j.epsl.2025.119622.

Data availability

Data is in a repository and a link is provided.

References

Alvero, M., Mazzucchelli, M.L., Angel, R.J., Murri, M., Campomenosi, N., Scambelluri, M., Nestola, F., Korsakov, A., Tomilenko, A.A., Marone, F., Morana, M., 2020. Fossil subduction recorded by quartz from the coesite stability field. Geology 48 (1), 24–28. https://doi.org/10.1130/G46617.1.

Asano, K., Michibayashi, K., Takebayashi, T., 2021. Rheological contrast between quartz and coesite generates strain localization in deeply subducted continental crust. Minerals 11, 842. https://doi.org/10.3390/min11080842.

Bachmann, F., Hielscher, R., Schaeben, H., 2010. Texture analysis with MTEX - free and open source software toolbox. Solid State Phenomena 160, 63–68. https://doi.org/10.4028/www.scientific.net/SSP.160.63.

Bestmann, M., Pennacchioni, G., Grasemann, B., 2021. Deformation-induced Japan twinning in quartz during incipient mylonitization. Geology 49, 1267–1271. https://doi.org/10.1130/G49077.1.

Bidgood, A.K., Parsons, A.J., Lloyd, G.E., Waters, D.J., Goddard, R.M., 2021. EBSD-based criteria for coesite-quartz transformation. J. Metamorph. Geol. 39 (2), 165–180. https://doi.org/10.1111/jmg.12566.

Bidgood, A.K., Parsons, A.J., Roberts, N.M., Waters, D., Tapster, S., Gopon, P., 2024. The geodynamic significance of continental UHP exhumation: new constraints from the Tso Morari Complex, NW Himalaya. Tectonics 43 (5), e2023TC007976. https://doi.org/10.1029/2023TC007976.

Campanale, F., Mugnaioli, E., Gemmi, M., Folco, L., 2021. The formation of impact coesite. Sci. Rep. 11, 16011. https://doi.org/10.1038/s41598-021-95432-6.

Castelli, D., Rolfo, F., Groppo, C., Compagnoni, R., 2007. Impure marbles from the UHP Brossasco-Isasca Unit (Dora-Maira Massif, western Alps): evidence for Alpine equilibrium in the diamond stability field and evaluation of the X(CO2) fluid evolution. J. Metamorph. Geol. 25 (6), 587–603. https://doi.org/10.1111/j.1525-1314.2007.00716.x.

Chopin, C., 1984. Coesite and pure pyrope in high-grade blueschists of the Western Alps: a first record and some consequences. Contrib. Minerol. Petrol. 86, 107–118. https://doi.org/10.1007/BF00381838.

Chopin, C., Schertle, H.P., 1999. The UHP unit in the Dora-Maira Massif, Western Alps. Int. Geol. Rev. 41 (9), 765–780. https://doi.org/10.1080/00206819909465168.

Cross, A.J., Goddard, R.M., Kumamoto, K.M., Goldsby, D.L., Hansen, L.N., Chen, H., Hein, D., Thom, C.A., Nehring, M.A., Breithaupt, T., Wallis, D., 2025. Direct observations of transient weakening during phase transformations in quartz and olivine. Nat. Geosci. 18, 548–554. https://doi.org/10.1038/s41561-025-01703-6.

Cutts, J., Dyck, B., 2022. Incipient collision of the Rae and Slave cratons at ca. 1.95 Ga. GSA Bull. 135 (3–4), 903–914. https://doi.org/10.1130/B36393.1.

Cutts, J., Dyck, B., Perrot, M.G., Davies, J.H.F.L., Osinchuk, A.M., Šilerová, D., Stern, R. A., Chiaradia, M., Canam, R., 2024. A contiguous Taltson-Thelon margin revisited. Geochem. Geophys. Geosyst. 25 (7), e2024GC011527. https://doi.org/10.1029/2024GC011527.

Dyck, B., Goddard, R.M., Wallis, D., Hansen, L.N., Martel, E., 2020. Metamorphic evolution of the Great Slave Lake shear zone. J. Metamorph. Geol. 39 (5), 567–590. https://doi.org/10.1111/jmg.12576.

Frondel, C., 1945. Secondary Dauphiné twinning in quartz. Am. Mineral. 30 (5–6), 447–460.

Gómez-Ramírez, R., Pound, G.M., 1973. Nucleation of a second solida phase along dislocations. Metall. Transc. 4, 1563–1570. https://doi.org/10.1007/BF02668009.

Ingrin, J., Gillet, P., 1986. TEM investigation of the crystal microstructures in a Quartz-Coesite assemblage of the Western Alps. Phys. Chem. Miner. 13, 325–330. https://doi.org/10.1007/BF00308349.

Kohn, M.J., 2014. Thermoba-Raman-try': calibration of spectroscopic barometers and thermometers for mineral inclusions. Earth. Planet. Sci. Lett. 388, 187–196. https://doi.org/10.1016/j.epsl.2013.11.054.

Langenhorst, F., Poirer, J.-P., 2002. Transmission electron microscope of coesite inclusions in the Dora Maira high-pressure metamorphic pyrope-quartzite. Earth. Planet. Sci. Lett. 203, 793–803. https://doi.org/10.1016/S0012-821X(02)00949-4.

Lathe, C., Koch-Müller, M., Wirth, R., van Westrenen, W., Mueller, H.J., Schilling, F., Lauterjung, J., 2005. The influence of OH in coesite on the kinetics of the coesite-quartz phase transition. Am. Mineral. 90, 36–43. https://doi.org/10.2138/am.2005.1662.

Lenart, A., Samardžija, Z., Godec, M., Mirtič, B., Šturm, S., 2012. Twin-boundary formation in Japan-law tinned quartz crystals. Eur. J. Mineral. 24 (3), 509–517. https://doi.org/10.1127/0935-1221/2012/0024-2202.

Lenze, A., Stöckhert, B., 2007. Microfabrics of UHP metamorphic granites in the Dora Maira Massif, western Alps — no evidence of deformation at great depth. J. Metamorph. Geol. 25 (4), 461–475. https://doi.org/10.1111/j.1525-1314.2007.00707.x.

Lenze, A., Stöckhert, B., 2008. Microfabrics of quartz formed from coesite (Dora-Maira Massif, Western Alps). Eur. J. Mineral. 20 (5), 811–826. https://doi.org/10.1127/0935-1221/2008/0020-1848.

Lenze, A., Stöckhert, B., Wirth, R., 2005. Grain scale deformation in ultra-high-pressure metamorphic rocks — an indicator of rapid phase transformation. Earth Planet. Sci. Lett. 299 (3–4), 217–230. https://doi.org/10.1016/j.epsl.2004.10.012.

Mainprice, D., Bachmann, F., Hielscher, R., Schaeben, H., 2015. Descriptive tools for the analysis of texture projects with large datasets using MTEX: strength, symmetry and components in *Rock Deformation from Field, Experiments, and Theory: a Volume in Honour of Ernie Rutter*. Geol. Soc. Lond. Spec. Publ. 409, 251–271. https://doi.org/10.1144/sp409.8.

Mosenfelder, J.L., Bohlen, S.R., 1997. Kinetics of the coesite to quartz transformation. Earth. Planet. Sci. Lett. 153 (1–2), 133–147. https://doi.org/10.1016/S0012-821X(97)00159-3.

Nagai, T., Ohtaka, O., Yamanaka, T., 1997. Kinetic studies of the α-quartz-coesite transformation of SiO_2. Mineral. J. 19 (4), 147–154. https://doi.org/10.2465/minerj.19.147.

Nolze, G., Hielscher, R., 2016. Orientations — perfectly colored. J. Appl. Crystallogr. 49, 1786–1802. https://doi.org/10.1107/S1600576716012942.

O'Brien, P.J., Zotov, N., Law, R., Khan, M.A., Jan, M.Q., 2001. Coesite in Himalayan eclogite and implications for models of India-Asia collision. Geology 29 (5), 435–438. https://doi.org/10.1130/0091-7613(2001)029<0435:CIHEAI>2.0.CO;2.

Parsons, A.J., Sigloch, K., Hosseini, K., 2021. Australian plate subduction is responsible for northward motion of the India-Asia collision zone and ~ 1000 km lateral migration of the Indian slab. Geophys. Res. Lett. 48 (18), e2021GL094904. https://doi.org/10.1029/2021GL094904.

Perrillat, J.P., Daniel, I., Lardeaux, J.M., Cardon, H., 2003. Kinetics of the Coesite–Quartz transition: application to the exhumation of ultrahigh-pressure rocks. J. Petrol. 44 (4), 773–788. https://doi.org/10.1093/petrology/44.4.773.

Poppa, H., 1963. In-situ studies of epitaxial thin-film growth. J. Phys. Sci. 19, 835–843. https://doi.org/10.1515/zna-1964-7-803.

Proyer, A., 2003. The preservation of high-pressure rocks during exhumation: metagranites and metapelites. Lithos 70 (3–4), 183–194. https://doi.org/10.1016/S0024-4937(03)00098-7.

Richter, B., Stünitz, H., Heilbronner, R., 2016. Stresses and pressures at the quartz-to-coesite phase transformation in shear deformation experiments. J. Geophys. Res. 121, 8015–8033. https://doi.org/10.1002/2016JB013084.

Rubie, D.C., Tsuchida, Y., Yagi, T., Utsumi, W., Kiregawa, T., Shimomura, O., Brearley, A. J., 1990. An in situ X ray diffraction study of the kinetics of the Ni_2SiO_4 olivine-spinel transformation. J. Geophys. Res. 95 (B10), 15829–15844. https://doi.org/10.1029/JB095iB10p15829.

Ruiz-Cruz, M.D., Sanz de Galdeano, C., 2012. Diamond and Coesite in Ultrahigh-pressure-ultrahigh-temperature granulites from Ceuta, Northern Rif, northwest Africa. Mineral. Mag. 76 (3), 683–705. https://doi.org/10.1180/minmag.2012.076.3.17.

Schertl, H.,-P., Schreyer, W., Chopin, C., 1991. The pyrope-coesite rocks and their country rocks at Parigi, Dora Maira Massif, Western Alps: detailed petrography, mineral chemistry and PT-Path. Contrib. Minerol. Petrol. 108, 1–21. https://doi.org/10.1007/BF00307322.

Shigematsu, N., Prior, D.J., Wheeler, J., 2006. First combined electron backscatter diffraction and transmission electron microscopy study of grain boundary structure of deformed quartzite. J. Microsc. 224 (3), 306–321. https://doi.org/10.1111/j.1365-2818.2006.01697.x.

Šilerová, D., Dyck, B., Cutts, J.A., Larson, K., 2023. Long-lived (180 Myr) ductile flow within the great slave lake shear zone. Tectonics 42 (9). https://doi.org/10.1029/2022TC007721.

Skemer, P., Katayama, I., Jiang, Z., Karato, S.-I., 2005. The misorientation index: development of a new method for calculating the strength of lattice-preferred orientation. Tectonophysics 411, 157–167. https://doi.org/10.1016/j.tecto.2005.08.023.

Smyth, J.R., 1977. Quartz pseudomorphs after coesite. Am. Mineral. 62, 828–830.

St-Onge, M.R., Rayner, N., Palin, R.M., Searle, M.P., Waters, D.J., 2013. Integrated pressure-temperature-time constraints for the Tso Morari dome (Northwest India): implications for the burial and exhumation path of UHP units in the western Himalayas. J. Metamorph. Geol. 31 (5), 469–504. https://doi.org/10.1111/jmg.12030.

Sunagawa, I., 1991. Quartz crystals twinned after Brazil and Japan laws: origin of their morphological and texture characteristics. J. Gemmol. Soc. Japan 20 (1–4), 23–36. https://doi.org/10.14915/gsjapan.20.1-4_23.

Sunagawa, I., Hiroyuki, I., Takada, M., Hoshino, Y., 2004. Morphogenesis of quartz crystal twinned after Japan Law. Eur. J. Mineral. 16 (1), 91–97. https://doi.org/10.1127/0935-1221/2004/0016-0091.

Yasuda, T., Sunagawa, I., 1982. X-ray topographic study of quartz crystals twinned according to Japan twin law. Phys. Chem. Miner. 8, 121–127. https://doi.org/10.1007/BF00311282.

Wang, Y., Durham, W.B., Getting, I.C., Weidner, D.J., 2003. The deformation-DIA: a new apparatus for high temperature triaxial deformation to pressures of up to 15 GPa. Rev. Sci. Instrum. 74, 3002–3011. https://doi.org/10.1063/1.1570948.

Warren, C.J., 2013. Exhumation of (ultra-) high-pressure terranes: concepts and mechanisms. Solid Earth 4, 75–92. https://doi.org/10.5194/se-4-75-2013.

Wheeler, J., Rebby, S.M., Cliff, R.A., 2001. Kinematic linkage between internal zone extension and shortening in more external units in the NW Alps. J. Geol. Soc. London. 158, 439–443. https://doi.org/10.1144/jgs.158.3.439.

White, J.S., 2014. Mineral mysteries: a twinning mystery in natural crystals. Rocks Min. 89 (4), 375–377. https://doi.org/10.1080/00357529.2014.904672.

Zinn, P., Hinze, E., Lauterjung, J., Wirth, R., 1997a. Kinetic and microstructural studies of the quartz-coesite phase transition. Phys. Chem. Earth 22 (1–2), 105–111. https://doi.org/10.1016/S0079-1946(97)00089-X.

Zinn, P., Lauterjung, J., Wirth, R., 1997b. Kinetic and microstructural studies of the crystallisation of coesite from quartz at high pressure. Z. Kristallogr. 212, 691–698. https://doi.org/10.1524/zkri.1997.212.10.691.

Zhou, Y., He, C., Song, J., Ma, S., Ma, J., 2005. An experimental study of quartz-coesite transition at differential stress. Chin. Sci. Bull. 50, 446–451. https://doi.org/10.1007/BF02897461.